

## CHAOS V: RECOMBINATION LINE CARBON ABUNDANCES IN M 101

EVAN D. SKILLMAN<sup>1</sup>, DANIELE A. BERG<sup>2,3</sup>, RICHARD W. POGGE<sup>2,3</sup>, JOHN MOUSTAKAS<sup>4</sup>, NOAH S. J. ROGERS<sup>1</sup>, AND KEVIN V. CROXALL<sup>2,5</sup><sup>1</sup>Minnesota Institute for Astrophysics, University of Minnesota, 116 Church St. SE, Minneapolis, MN 55455<sup>2</sup>Department of Astronomy, The Ohio State University, 140 W 18th Ave., Columbus, OH, 43210<sup>3</sup>Center for Cosmology & AstroParticle Physics, The Ohio State University, 191 West Woodruff Avenue, Columbus, OH 43210<sup>4</sup>Department of Physics & Astronomy, Siena College, 515 Loudon Road, Loudonville, NY 12211<sup>5</sup>Illumination Works LLC, 5550 Blazar Parkway #150, Dublin, OH 43017, USA 0000-0002-5258-7224

(Accepted to ApJ)

## ABSTRACT

The CHAOS project is building a large database of LBT H II region spectra in nearby spiral galaxies to use direct abundances to better determine the dispersion in metallicity as a function of galactic radius. Here, we present CHAOS LBT observations of C II  $\lambda 4267$  emission detected in 10 H II regions in M 101, and, using a new photoionization model based ionization correction factor, we convert these measurements into total carbon abundances. A comparison with M 101 C II recombination line observations from the literature shows excellent agreement, and we measure a relatively steep gradient in  $\log(C/H)$  of  $-0.37 \pm 0.06$  dex  $R_c^{-1}$ . The C/N observations are consistent with a constant value of  $\log(C/N) = 0.84$  with a dispersion of only 0.09 dex, which, given the different nucleosynthetic sources of C and N, is challenging to understand. We also note that when plotting N/O versus O/H, all of the H II regions with detections of C II  $\lambda 4267$  present N/O abundances at the minimum of the scatter in N/O at a given value of O/H. If the high surface brightness necessary for the detection of the faint recombination lines is interpreted as an indicator of H II region youth, then this may point to a lack of nitrogen pollution in the youngest H II regions. In the future, we anticipate that the CHAOS project will significantly increase the total number of C II  $\lambda 4267$  measurements in extragalactic H II regions.

*Subject headings:* galaxies: individual (M 101) — galaxies: ISM — ISM: lines and bands

## 1. INTRODUCTION

1.1. *The Nucleosynthetic Production of Carbon*

The production of carbon is a relatively complex topic (cf. Henry et al. 2000). Although carbon is produced primarily through the triple- $\alpha$  process, there are multiple sites where this process can take place and the balance between carbon production and oxygen production has dependencies on both nuclear physics and astrophysics (cf., Arnett 1996). Models of the chemical evolution in our galaxy indicate that massive stars and intermediate mass stars have played roughly equal roles in the production of carbon in the solar vicinity (Carigi et al. 2005).

Carbon clearly has at least two sites of production relevant to the chemical evolution of galaxies. The relatively flat relationship between C/O and O/H observed at low metallicities (e.g., Garnett et al. 1995, 1997; Izotov & Thuan 1999; Esteban et al. 2014; Berg et al. 2016, 2019) is indicative of a primary production process in massive stars (e.g., Woosley & Weaver 1995). The observed increase in the C/O ratio with increasing metallicity (e.g., Garnett et al. 1999; Esteban et al. 2005, 2009, 2019) indicates that secondary-like production becomes important at higher metallicities. Although this is similar to the observed trend of increasing N/O with increasing metallicity, that relationship is understood as a direct consequence of the CNO cycle. There is no similar nucleosynthetic process for the production of C, so the observed relative constancy of C/N is suggestive of a physical conspiracy of sorts. The increase of C/O with increasing O/H has been attributed to both an increasing yield of C in massive stars with increasing metallicity

due to strengthening of stellar winds (e.g., Maeder 1992; Meynet & Maeder 2002; Hirschi et al. 2005), and metallicity dependent yields of intermediate mass stars (e.g., van den Hoek & Groenewegen 1997).

Carbon abundances in unevolved Galactic stars have the promise of tracing the evolution of both absolute and relative abundances as a function of time and place within our galaxy (e.g., Nissen et al. 2014), and carbon abundances in evolved stars can trace the nucleosynthetic processes involved with the later stages of stellar evolution (e.g., Henry et al. 2018; Feuillet et al. 2018; Hasselquist et al. 2019). Alternatively, carbon abundances from the ISM provide only the cumulative endpoint of all nucleosynthesis, gas flows, and mixing, but their observation can still give constraints on the chemical evolution of galaxies. Hopefully these constraints can lead to a better understanding of the dominant carbon production processes. Here we will present ISM carbon abundances derived from carbon recombination lines.

1.2. *The Abundance Discrepancy Factor (ADF)*

Because there are no strong collisionally excited lines from carbon in the optical regime, carbon abundance determinations in H II regions are very limited. The two most popular alternatives are the collisionally excited semi-forbidden lines of CIII] at  $\lambda\lambda 1907, 1909$  in the ultraviolet (e.g., Garnett et al. 1995; Berg et al. 2016, 2019) and the C II recombination line at  $\lambda 4267$  (e.g., Esteban et al. 1998, 2002, 2005; Peimbert et al. 2005; Bresolin 2007; Esteban et al. 2009, 2014; Toribio San Cipriano et al. 2016, 2017; Esteban et al. 2019). The primary observational challenge of observing the collisionally excited ul-

TABLE 1  
M 101 H II REGIONS WITH CHAOS C II  $\lambda$ 4267 DETECTIONS

$\frac{R}{R_{25}}$	H II Region Name	CHAOS ID <sup>a</sup>	$I(\text{C II } \lambda 4267)/I(\text{H}\beta)$	T[O III] (K) <sup>a</sup>	T[S III] (K) <sup>a</sup>
0.196	H1013 <sup>b</sup>	+164.6+009.9	0.0023 $\pm$ 0.0003	7420 $\pm$ 180	6910 $\pm$ 110
0.284	H1052 <sup>b</sup>	+189.2–136.3	0.0029 $\pm$ 0.0002	7769 $\pm$ 77	8900 $\pm$ 160
0.335	NGC 5461	+254.6–107.2	0.0013 $\pm$ 0.0004	8739 $\pm$ 66	9340 $\pm$ 320
0.426	NGC 5462	+354.1+071.2	0.0009 $\pm$ 0.0003	9542 $\pm$ 90	8190 $\pm$ 260
0.435	NGC 5462	+360.9+075.3	0.0013 $\pm$ 0.0003	9179 $\pm$ 93	8030 $\pm$ 280
0.468	NGC 5455	–099.6–388.0	0.0010 $\pm$ 0.0002	9443 $\pm$ 70	8920 $\pm$ 210
0.541	NGC 5447	–368.3–285.6	0.0011 $\pm$ 0.0002	9299 $\pm$ 69	11150 $\pm$ 270
0.554	NGC 5447	–392.0–270.1	0.0012 $\pm$ 0.0004	9579 $\pm$ 75	11200 $\pm$ 290
0.669	H1216 <sup>b</sup>	+509.5+264.1	0.0004 $\pm$ 0.0004	10692 $\pm$ 88	9930 $\pm$ 240
0.813	NGC 5471	+667.9+174.1	0.0004 $\pm$ 0.0003	12790 $\pm$ 170	12110 $\pm$ 410

<sup>a</sup> from Croxall et al. (2016)

<sup>b</sup> naming convention from Hodge et al. (1990)

traviolet lines, beyond needing space-based observations, is the lack of a nearby hydrogen emission line to use as a reference. The solution to this is to compare to the nearby OIII] lines at  $\lambda\lambda$  1660, 1666. The primary observational challenge for the optical recombination lines is the intrinsic extreme weakness of the lines which are typically observed at  $\sim 0.1\%$  of  $\text{H}\beta$  (with a roughly linear dependence on O/H).

However, with sufficient sensitivity to observe the C recombination line, a second difficulty arises. In principle, absolute ionic abundances from recombination lines should be very robust because of the negligible dependence on temperature when converting from line flux ratios to abundances. However, whenever recombination line ionic abundances are compared to ionic abundances derived from collisionally excited lines (most frequently for  $\text{O}^{++}$  and  $\text{C}^{++}$ ) an “abundance discrepancy factor” (ADF) with an amplitude of roughly a factor of two is found (in the sense that the recombination lines produce higher abundances, cf. García-Rojas & Esteban 2007). Given the inherent bias to higher values in the determination of temperatures from auroral-to-nebular flux ratios of collisionally excited lines (the basis of the “direct” abundance method) and the high temperature sensitivity of the relative strengths of the collisionally excited lines, the most natural explanation for the ADF is that there are temperature fluctuations in the H II regions (e.g., Peimbert 1967; Peimbert & Costero 1969). Note that this explanation is currently debated in the literature; the most common criticism is that the size of the temperature fluctuations required to explain the observed ADF is larger than can easily be reproduced in photoionization models (e.g., Simón-Díaz & Stasińska 2011; Stasińska et al. 2013).

In this paper, we will derive ionic  $\text{C}^{++}/\text{H}^+$  abundances from the C II  $\lambda$ 4267 line and then convert the ionic abundance to a total abundance, C/H, via ionization corrections based on photoionization modeling. We also reference our derived C/H values to previously reported O/H and N/H values derived from collisionally excited lines using the direct method. Because the  $\text{C}^{++}/\text{H}^+$  ADF is of order a factor of two (e.g., Toribio San Cipriano et al. 2017), our C/O and C/N ratios are expected to be offset upward by roughly a similar factor of two when comparing them to ratios determined purely from recombination lines or collisionally excited lines.

### 1.3. CHAOS Observations of M 101

While numerous spectra of star forming galaxies have been obtained through large surveys such as SDSS (Strauss et al. 2002; Tremonti et al. 2004), PINGS (Rosales-Ortega et al. 2010), CALIFA (Sánchez et al. 2012), MaNGA (Bundy et al. 2015; Law et al. 2015), SAMI (Bryant et al. 2015), TYPHOON (e.g., Ho et al. 2017), and PHANGS-MUSE (Kreckel et al. 2019), few of these observations enable direct determinations of absolute gas-phase abundances, as they do not detect the faint auroral lines that reveal the electron temperatures of the H II regions. Even determining the relative abundances can be challenging given possible biases, both in the observations and the methodology of determining gas-phase metallicity using only the brightest lines (Kewley & Ellison 2008). Furthermore, the coarse spatial resolution that results from observing distant galaxies means that non-homogeneous clouds of gas will co-inhabit each spectrum (Moustakas & Kennicutt 2006). The goal of the CHEMICAL Abundances Of Spirals (CHAOS) program is to obtain very high quality spectra of H II regions in nearby spiral galaxies, which allow direct determinations of absolute and relative abundances across a broad range of parameter space (e.g., Berg et al. 2015). The CHAOS program uses the Multi-Object Double Spectrographs (MODS, Pogge et al. 2010) on the Large Binocular Telescope (LBT, Hill 2010) to observe large numbers of H II regions in spiral galaxies. Recognizing that direct abundances do have systematic biases (e.g., Peimbert 1967; Stasińska 2005), our goal is to obtain a very large sample of direct abundances as a best chance to assess those systematics.

The nearly face-on spiral galaxy M 101 (NGC 5457), with its relatively steep metallicity gradient, is an ideal target for H II region observations and has been observed several times (e.g., Kennicutt et al. 2003; Bresolin 2007; Li et al. 2013; Esteban et al. 2019). As part of CHAOS, Croxall et al. (2016) presented observations of 74 H II regions in M 101 with direct abundances. Although it was not an original goal of the CHAOS project, we realized that our observations were sensitive enough to detect the C II  $\lambda$ 4267 recombination line in a number of our spectra. Here we present an analysis of those observations.

Our observations and data reduction are described in §2. In §3 we determine gas-phase chemical abundances. We present abundance gradients for C/H, C/O, and C/N in §4. We discuss relative abundances and the origin of C in §5. Finally, we summarize our conclusions in §6. We will assume the same properties for M 101 as in

TABLE 2  
 M 101 CHAOS H II REGION CARBON ABUNDANCES

$\frac{R}{R_{25}}$	Region Name	$C^{++}/H^+$ $\times 10^{-5}$	$O^{++}/O^a$	C/H ICF	$12+\log(C/H)$	$\log(C/O)$	$\log(C/N)$	$12+\log(O/H)^a$
0.196	H1013	$18.3 \pm 2.2$	$0.30 \pm 0.02$	$0.54 \pm 0.05$	$8.53 \pm 0.06$	$-0.04 \pm 0.07$	$0.92 \pm 0.08$	$8.57 \pm 0.02$
0.284	H1052	$23.7 \pm 1.5$	$0.66 \pm 0.02$	$0.76 \pm 0.05$	$8.49 \pm 0.04$	$-0.08 \pm 0.04$	$0.93 \pm 0.05$	$8.57 \pm 0.01$
0.335	NGC 5461	$11.2 \pm 2.9$	$0.66 \pm 0.03$	$0.76 \pm 0.05$	$8.17 \pm 0.12$	$-0.31 \pm 0.12$	$0.69 \pm 0.13$	$8.48 \pm 0.02$
0.426	NGC 5462	$7.6 \pm 2.9$	$0.51 \pm 0.06$	$0.66 \pm 0.06$	$8.06 \pm 0.18$	$-0.39 \pm 0.19$	$0.81 \pm 0.21$	$8.45 \pm 0.05$
0.435	NGC 5462	$10.5 \pm 2.7$	$0.64 \pm 0.02$	$0.74 \pm 0.05$	$8.15 \pm 0.12$	$-0.28 \pm 0.12$	$0.90 \pm 0.13$	$8.43 \pm 0.01$
0.468	NGC 5455	$8.7 \pm 2.0$	$0.70 \pm 0.03$	$0.79 \pm 0.05$	$8.04 \pm 0.11$	$-0.34 \pm 0.11$	$0.81 \pm 0.13$	$8.39 \pm 0.02$
0.541	NGC 5447	$9.1 \pm 1.8$	$0.56 \pm 0.02$	$0.69 \pm 0.05$	$8.12 \pm 0.09$	$-0.30 \pm 0.09$	$0.83 \pm 0.10$	$8.42 \pm 0.01$
0.554	NGC 5447	$9.8 \pm 3.6$	$0.69 \pm 0.02$	$0.78 \pm 0.05$	$8.10 \pm 0.17$	$-0.25 \pm 0.17$	$0.88 \pm 0.18$	$8.35 \pm 0.01$
0.669	H1216	$3.3 \pm 3.3$	$0.65 \pm 0.05$	$0.75 \pm 0.06$	$7.64 \pm 0.50$	$-0.63 \pm 0.50$	$0.70 \pm 0.50$	$8.26 \pm 0.03$
0.813	NGC 5471	$4.0 \pm 3.1$	$0.78 \pm 0.05$	$0.85 \pm 0.05$	$7.67 \pm 0.46$	$-0.47 \pm 0.46$	$0.90 \pm 0.50$	$8.14 \pm 0.03$

<sup>a</sup> from Croxall et al. (2016)

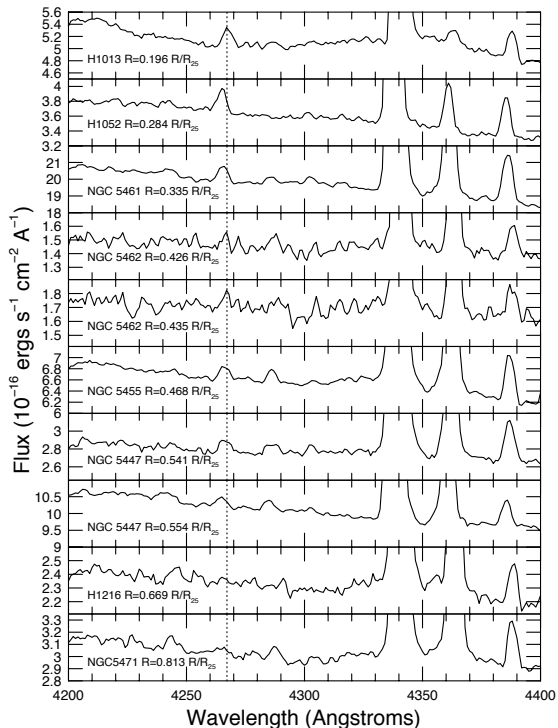


FIG. 1.— CHAOS spectra of the M101 H II regions, where the C II  $\lambda 4267$  recombination line was detected, zoomed in to the region surrounding that line. The  $\lambda 4267$  line is marked with a vertical dotted line. The three strong lines at longer wavelengths are H I  $\lambda 4340$ , [O III]  $\lambda 4363$ , and He I  $\lambda 4388$ . The spectra are arranged in increasing galactocentric radius from top to bottom. Note that, at this scaling, the He I  $\lambda 4388$  line is relatively constant while the C II  $\lambda 4267$  line becomes weaker with increasing radius (decreasing metallicity) and the [O III]  $\lambda 4363$  line becomes stronger with increasing radius.

Croxall et al. (2016), i.e., a distance of 7.4 Mpc (Ferrarese et al. 2000) (with a resulting scale of 35.9 pc/arcsec),  $R_{25} = 864''$  (Kennicutt et al. 2011), an inclination angle of  $18^\circ$ , and a major-axis position angle of  $39^\circ$  (Walter et al. 2008). We also use a value for  $R_e$  of  $198''$  (Berg et al. 2020).

## 2. CHAOS SPECTRA AND REDUCTIONS

The observations presented here were previously reported in Croxall et al. (2016) and we provide a brief summary. Optical spectra of M 101 were taken using MODS on the LBT during the spring semester of 2015. All spectra were acquired with the MODS1 unit. We

obtained simultaneous blue and red spectra using the G400L (400 lines  $\text{mm}^{-1}$ ,  $R \approx 1850$ ) and G670L (250 lines  $\text{mm}^{-1}$ ,  $R \approx 2300$ ) gratings, respectively. The main goal of this program was to detect the intrinsically weak auroral lines in the wavelength range from 3200–10,000 Å in order to obtain direct abundances. Although not a design goal of the program, the observations were sensitive enough to detect recombination line emission from the C II recombination line at  $\lambda 4267$ . Recombination line observations are normally made at higher spectral resolution than in the CHAOS program, but because the C II  $\lambda 4267$  is well isolated, these detections are possible.

Figure 1 shows the wavelength region of the spectra highlighting the C II  $\lambda 4267$  emission line for the 10 H II regions in M 101 where it was detected. Previously, in the CHAOS program, we have limited reporting of detections to a minimum signal/noise cutoff of 3. Because of the extreme faintness of the C II  $\lambda 4267$  emission line and the very high worth of any detections, we have dropped that constraint (as is customary in the recombination line literature, e.g., Esteban et al. 2009) for the two lowest metallicity detections. However, instead of marking reported weak detections with colons, we have reported our best estimates of the uncertainties of the measurements. Note also that in two cases, two of our observations are independent regions in large H II region complexes (i.e., NGC 5462 and NGC 5447).

We also searched the spectra for the presence of O II multiplet 1 recombination lines (e.g.,  $\lambda\lambda$  4639, 4642, 4649, 4651, 4662, 4674, 4676), but here our relatively low spectral resolution of  $\sim 2$  Å limited our sensitivity to these lines. Not only were some of these lines confused with emission from N III at  $\lambda 4641$  and [Fe III] at  $\lambda 4658$ , but broad Wolf-Rayet “blue bump” emission between  $\lambda$  4630 and 4700 Å was detected in all of the spectra in which C II  $\lambda 4267$  emission was detected. As a result, we cannot report any C/O measurements based solely on recombination lines.

Detailed descriptions of the data reduction procedures are provided in Berg et al. (2015) and Croxall et al. (2016). The measurements of the C II  $\lambda 4267$  emission lines were made identically to the measurements reported in Croxall et al. (2016). The C II  $\lambda 4267$  line was not measured as part of the original CHAOS pipeline because we did not anticipate very many detections. For the analysis here, we use the de-reddened relative emission line strengths reported in Croxall et al. (2016) and the physi-

cal conditions (e.g., temperatures and densities) reported therein. Given the weakness of the line, the associated uncertainty is dominated by photon counting statistics. In Table 1, we report locations of the H II regions where C II  $\lambda 4267$  has been detected, the reddening corrected C II  $\lambda 4267$  emission line fluxes relative to  $H\beta$ , and the [O III] and [S III] temperatures from Croxall et al. (2016).

In the top panel of Figure 2, we plot our C II  $\lambda 4267$  emission line fluxes relative to  $H\beta$  as a function of the deprojected distances from the galaxy center in units of the isophotal radius,  $R_{25}$  (Croxall et al. 2016). Because of the weak dependence on temperature, the  $\lambda 4267/H\beta$  ratio directly reflects the  $C^{++}/H^+$  ratio and one immediately sees evidence of the strong radial gradient. We have added to this plot the other published observations of C II  $\lambda 4267$  emission in M 101 for comparison (Esteban et al. 2002; Bresolin 2007; Esteban et al. 2009, 2019). The top panel of Figure 2 shows the excellent agreement of our observations with the ten previously published detections in six distinct H II regions (for consistency, we have used the radial distances adopted in this work). In sum, we have added four C II  $\lambda 4267$  observations of H II regions lacking prior detections and C II  $\lambda 4267$  observations for two of these regions were subsequently reported by Esteban et al. (2019).

### 3. GAS-PHASE CARBON ABUNDANCES

#### 3.1. Ionic Abundances

The  $\lambda 4267/H\beta$  ratios can be converted directly to  $C^{++}/H^+$  ratios with knowledge of their respective emissivities. Davey et al. (2000) have calculated recombination coefficients for C II lines, and in their Table 5, they provide polynomial fits at an electron density of  $10^4 \text{ cm}^{-3}$  over the temperature range of 5,000K to 20,000K. We use their Case B formula for making our calculations. Hummer & Storey (1987) have calculated the corresponding recombination coefficients for H I. Although the H II regions in M 101 are observed to have lower densities than the  $10^4 \text{ cm}^{-3}$  used in the emissivity calculations, the effective recombination coefficient is not very sensitive to density at these temperatures (Davey et al. 2000). In our calculations, we do not attribute uncertainties to the atomic data as the observational uncertainties are considered to be much larger. Although assessing uncertainties on atomic data from calculations can be difficult, our assumption is based mostly on the report by Davey et al. (2000) that a comparison of the effective recombination coefficient for the C II  $\lambda 4267$  line with the earlier calculation by Pequignot et al. (1991) agrees within 2.4%. Note also, that if the cause of the ADF is nebular temperature fluctuations, and if a significant amount of the recombination line emission is produced in significantly cooler regions than measured by the auroral to nebular line ratios, then the temperature range of 5,000K to 20,000K of the calculations by Davey et al. (2000) may be inadequate.

Although the temperature dependence of the conversion from flux ratio to ionic abundance is quite small (roughly a 10% variation over the temperature range of the H II regions), a nebular temperature is required to make the calculation. The natural temperature to use would be that derived from the [O III]  $\lambda 4363/\lambda 5007$  ratio. Since there has been some speculation regarding

the reliability of nebular temperatures derived from the [O III]  $\lambda 4363/\lambda 5007$  ratio (e.g., Binette et al. 2012; Berg et al. 2015, 2020), we report in Table 1 the T[O III] and T[S III] values for each of the H II regions calculated by Croxall et al. (2016). From Table 1 it can be seen that, although the measurements differ by many times their statistical uncertainties, there is coarse agreement between the two measurements. Most importantly, given the relatively large observational uncertainties on the recombination lines and the very low dependence of the abundances on the electron temperature, the choice of temperature will not have any impact. For simplicity, we have chosen to use T[O III] for this calculation. The values of  $C^{++}/H^+$  and their uncertainties are reported in Table 2.

#### 3.2. Ionization Correction Factors and Total Abundances

Ionization correction factors (ICFs) are required to convert our  $C^{++}/H^+$  measurements to values of C/H. Because of the small variations in the ionization correction for converting  $C^{++}/O^{++}$  to C/O (Garnett et al. 1995; Berg et al. 2016, 2019; Esteban et al. 2019), and the relative robustness of nebular O/H measurements, one possible choice would be to compare our  $C^{++}/H^+$  measurements to  $O^{++}/H^+$  measurements and to then convert  $C^{++}/O^{++}$  to C/O, which can then be multiplied by O/H to obtain the C/H ratio. This is the method typically used when observing both  $C^{++}$  and  $O^{++}$  in either optical recombination lines or ultraviolet collisionally excited lines. This would be possible here, although the resultant C/O would come from a mix of recombination lines and collisionally excited lines (because we have no  $O^{++}$  recombination line observations).

Alternatively, we can use the ionization corrections derived from photoionization models to go directly from  $C^{++}/H^+$  to C/H. Figure 3 shows an expanded grid of models from that reported in Berg et al. (2019) which was investigated to judge the stability of the corresponding ICF. We found that this ICF is very well behaved over the oxygen fractional ionization interval  $0.05 < O^{+2}/(O^{+} + O^{+2}) < 0.95$ , over a large range of metallicities and H II region ages, with a dispersion in the models of only 4.4%. In this range, the ICF varies smoothly from  $\sim 0.3$  to  $\sim 0.9$ . While this range in ICF is larger than the the range of ICFs based on  $C^{++}/O^{++}$ , the strong stability of the ICF over this range in oxygen fractional ionization gives us confidence that this is a satisfactory choice. From this photoionization modeling, we derive the following relationship:

$$C^{+2}/H^+ = 0.101 + 2.849x - 7.077x^2 + 9.356x^3 - 4.358x^4 \quad (1)$$

where  $x$  is the oxygen fractional ionization  $= O^{+2}/(O^{+} + O^{+2})$ . The ICFs are reported in Table 2 along with the corresponding values of  $\log(C/H)$ . The uncertainties on the ICFs represent both the observational uncertainties on the values of the ionization fractions of oxygen (which are required to calculate the ICFs) and the dispersion in photoionization models, added in quadrature.

With values of C/H, we can then multiply by our previously calculated values of O/H and N/H to obtain C/N and C/O, which are also tabulated in Table 2. Note that because the O/H and N/H values are calculated from col-

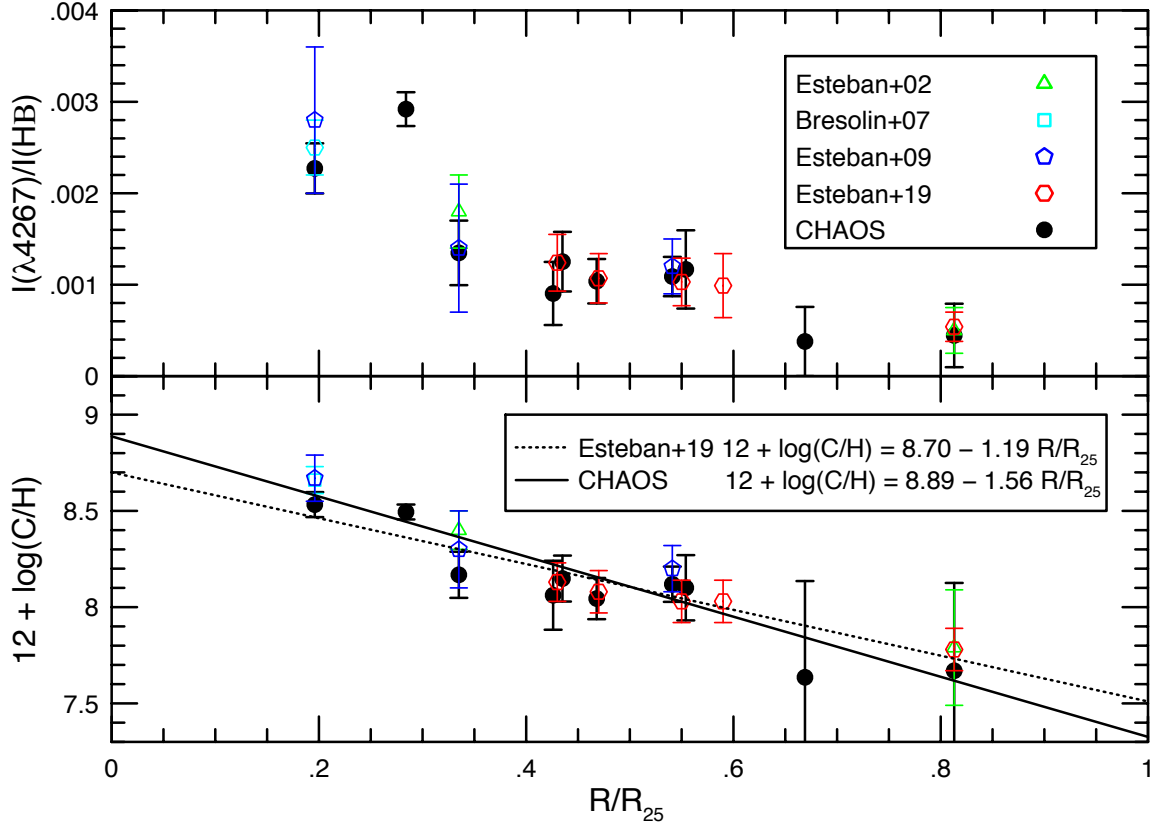


FIG. 2.— The top panel shows our C II  $\lambda 4267/\text{H}\beta$  observations in 10 M 101 H II regions plotted as a function of radius. We have included previously published observations (from Esteban et al. 2002; Bresolin 2007; Esteban et al. 2009, 2019) for comparison. The agreement with previous observations is very good. In the bottom panel we plot the corresponding values of  $\log(\text{C}/\text{H})$  as a function of radius. The bottom panel also shows a comparison to the values of  $\log(\text{C}/\text{H})$  from the literature. The solid line shows a fit to the CHAOS data and the dotted line shows the fit from Esteban et al. (2019).

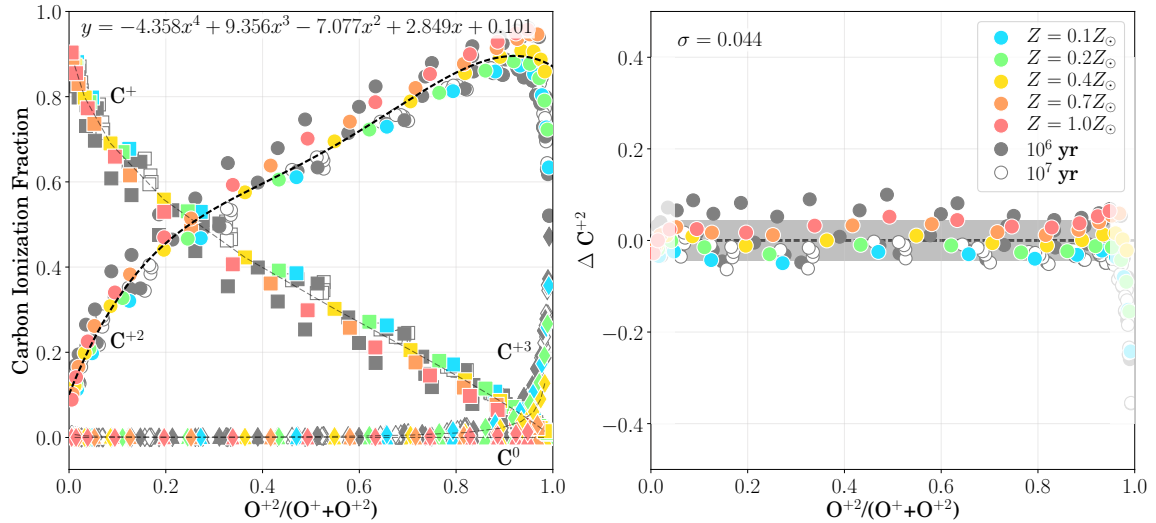


FIG. 3.— Left panel: C species ionization fractions as a function of  $\text{O}^{+2}$  ionization fraction for the purpose of calculating C ionization correction factors. Grey symbols designate deviations due to burst age ranging from  $t = 10^6$  (filled symbols) to  $t = 10^7$  (open symbols) years. Solid symbols are color-coded by the gas-phase oxygen abundance at  $t = 10^{6.7}$  yr. The different ionic species are designated by triangles, squares, circles, and diamonds in order of increasing ionization. Dashed gray lines connect the  $Z = 0.4 Z_{\odot}$  models, or  $12 + \log(\text{O}/\text{H}) = 8.3$ , which is a typical nebular abundance for our sample. Right panel: The dispersion in  $\text{C}^{+2}$  ionization fraction as a function of  $\text{O}^{+2}$  ionization fraction for all of the models presented in the left panel. The total dispersion is 0.044 from  $0.05 \leq \text{O}^{+2}/\text{O} \leq 0.95$ .

tionally excited lines and the C/H values from recombination lines, that the resulting C/O and C/N values are roughly 0.3 dex higher than values typically reported in the literature (cf. Esteban et al. 2019). We are also not making any corrections for dust. Although both carbon and oxygen are known to be depleted onto dust grains, typically the corrections for both are of order 0.1 dex. For example, in the comprehensive study by Esteban et al. (1998), the upward gas abundance to gas-plus-dust abundance corrections for the Orion nebula are 0.10 dex for carbon and 0.08 dex for oxygen. In the study of absorption in Milky Way lines of sight by Jenkins (2004) the relative ease with which an individual element depletes are nearly identical for C and O (in Jenkins’ formalism,  $-0.097$  versus  $-0.089$ ), although the offset from these relations is  $\sim 0.1$  dex higher for C than for O ( $-0.148$  versus  $-0.050$ ). So, very generally, the gas-phase C/O ratio is probably indicative of the total C/O ratio, but there is a fair degree of uncertainty in this assumption.

#### 4. ABUNDANCE GRADIENTS

##### 4.1. The C/H Abundance Gradient

A minimum number of H II regions spanning a significant fraction of the disk are required to produce an accurate measurement of an abundance gradient (e.g., Zaritsky et al. 1994; Skillman et al. 1996; Rosolowsky & Simon 2008; Bresolin et al. 2009b; Moustakas et al. 2010). With 10 H II regions spanning from 0.2 to 0.8 in  $R/R_{25}$ , we have sufficient observations to significantly constrain abundance gradients. However, at the largest radii, the uncertainties on the very weak detections of the C II  $\lambda 4267$  line do mitigate the constraints on the abundance gradients. Note that the recent measurement of C/H in NGC 5471 by Esteban et al. (2019) has a vastly improved uncertainty. Additional measurements of the ultraviolet C III] in the outer M101 regions would be welcome in this regard (although the ADF would need to be accounted for).

In the bottom panel of Figure 2 we have plotted  $\log(C/H)$  as a function of galactic radius. From a weighted fit to the CHAOS data we find:

$$12 + \log(C/H) = \begin{aligned} &8.89(\pm 0.09) - 1.56(\pm 0.25) (R/R_{25}) \\ &8.89(\pm 0.09) - 0.050(\pm 0.008) (R/\text{kpc}) , \\ &8.89(\pm 0.09) - 0.37(\pm 0.06) (R/R_e) \end{aligned} \quad (2)$$

and we have plotted this relationship as a solid line in Figure 2.

We have also plotted the previously reported values of  $\log(C/H)$  from the literature (Esteban et al. 2002; Bresolin 2007; Esteban et al. 2009, 2019). As should follow from the agreement with the observed fluxes, the derived values of  $\log(C/H)$  are in good agreement. Note that for the innermost H II region, H1013, where the CHAOS value of  $8.53 \pm 0.06$  is lower than the  $8.67 \pm 0.12$  previously reported by Esteban et al. (2009), that Esteban et al. (2019) have calculated a new value of  $8.58 \pm 0.11$  by applying a new ICF, resulting in agreement. Similarly, for NGC 5461, the CHAOS value of  $8.17 \pm 0.12$  is in agreement with the value of  $8.21 \pm 0.16$  which was revised down from the original report of  $8.30 \pm 0.20$  in Esteban et al. (2009). Overall, this indicates that our CHAOS measurements, although obtained at a lower spectral resolution, are capable of delivering quality C/H

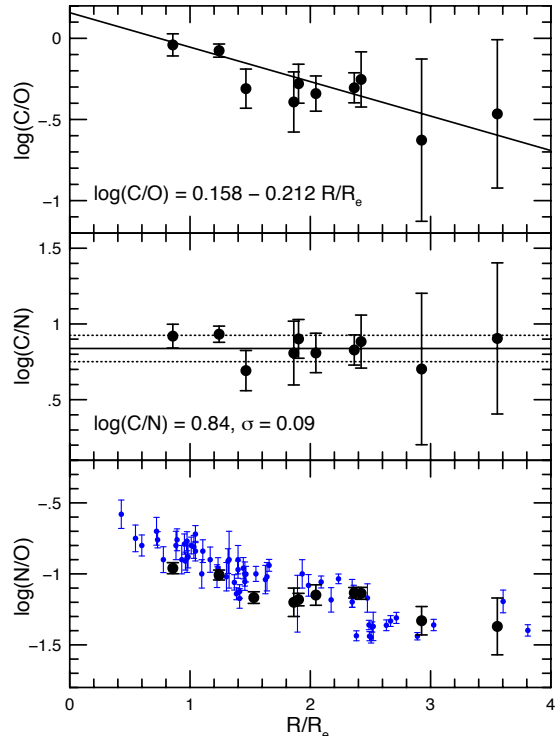


FIG. 4.— Radial abundance gradients of C/O, C/N, and N/O in M101. The top two panels show the results from our C II  $\lambda 4267$  observations. The bottom plot shows the N/O values presented in Croxall et al. (2016) with the black color coding indicating where we have detected C II  $\lambda 4267$  and all other points indicated in blue. The bottom plot shows that the regions detected in C II  $\lambda 4267$  are representative of the whole sample.

abundances.

Esteban et al. (2009) derived a linear best fit to the radial gradient of C/H in M101 of  $12 + \log(C/H) = 8.90 - 1.32 (\pm 0.33) R/R_{25}$ , in agreement with our value. Esteban et al. (2019) find  $12 + \log(C/H) = 8.70 (\pm 0.10) - 1.19 (\pm 0.19) R/R_{25}$ , with the lower intercept and slope, relative to the earlier result of Esteban et al. (2009), due, in part, to the lowering of the C/H abundances in their inner two H II regions and the very small uncertainty in their new measurement of NGC 5471. We have added the C/H radial gradient from Esteban et al. (2019) to Figure 2 as a dotted line. As expected from the agreement between the measurements, the gradients are in agreement. For all future comparisons to literature data in this paper, we will compare solely to the Esteban et al. (2019) results.

##### 4.2. Relative Abundance Gradients

In Figure 4, we plot the radial gradients for the C/O, C/N, and N/O abundance ratios from the CHAOS H II regions in M101. In Figure 4, we have switched from using  $R/R_{25}$  to  $R/R_e$  on the abscissa because of the evidence for more universal behavior of radial abundance gradients when comparing galaxy gradients based on the effective radius. Indeed, Sánchez et al. (2014) and Sánchez-Menguiano et al. (2016) have proposed a characteristic oxygen abundance gradient in spiral galaxies when measured in terms of the half-light or effective radius (but see also Sánchez-Menguiano et al. 2018), and Berg et al. (2020) have shown evidence for similar slopes in N/O.

In the top two panels of Figure 4, we plot the data made possible by the new measurements. The bottom panel reproduces the values from Croxall et al. (2016) for all of the M 101 H II regions with direct abundances. Comparing the radial distribution coverage in the top two panels with that in the bottom panel demonstrates that we have been able to sample most of the observable disk of M 101 with our C II  $\lambda 4267$  observations.

In the top panel of Figure 4, we see that  $\log(\text{C/O})$  has a significant negative gradient and a weighted linear fit yields

$$12 + \log(\text{C/O}) = \begin{aligned} &0.158(\pm 0.087) - 0.212(\pm 0.057) (R/R_{25}) \\ &0.158(\pm 0.087) - 0.0068(\pm 0.0018) (R/\text{kpc}) \\ &0.158(\pm 0.087) - 0.048(\pm 0.013) (R/R_e) \end{aligned} \quad (3)$$

This  $\log(\text{C/O})$  gradient is different from the value of  $\log(\text{C/O}) = -0.16 (\pm 0.24) - 0.40 (\pm 0.46) R/R_{25}$  found by Esteban et al. (2019), but that is to be expected because our O/H values are based on observations of collisionally excited lines. The intercept is higher because of the expected  $\sim 0.3$  dex offset between the direct and the recombination line O/H values. The smaller slope reflects a metallicity dependence in these values, although the slopes are consistent within the uncertainties.

In contrast, the middle panel of Figure 4 shows that  $\log(\text{C/N})$  is consistent with a constant value. The unweighted mean value of  $\log(\text{C/N})$  is 0.84 with a dispersion of 0.09 dex (the weighted mean is nearly identical at 0.86). This relatively constant value of C/N over a significant range in metallicity presents a challenge to explain given the different nucleosynthetic sources of C and N.

The relative constancy of  $\log(\text{C/N})$  means that  $\log(\text{C/O})$  and  $\log(\text{N/O})$  should have similar dependencies. This is not immediately obvious from a comparison of the top and bottom panels of Figure 4. The data for  $\log(\text{N/O})$ , shown in the bottom panel of Figure 4, are characterized by a decline with increasing radius followed by a relative flattening at large radii, while the data for  $\log(\text{C/O})$  appear to be well described by a linear fit. However, considering the lack of C/H measurements in the inner  $0.20 R/R_{25}$  and the small number of outer points (two) with relatively large uncertainties on the measurements of  $\log(\text{C/O})$ , the data are certainly consistent with a flattening in  $\log(\text{C/O})$  at larger radii. The new measurement in NGC 5471 by Esteban et al. (2019) is interesting in this regard because of the smaller uncertainty which does, indeed, favor a flattening the C/O radial gradient in M 101.

## 5. RELATIVE ABUNDANCE TRENDS

### 5.1. Trends with metallicity

In Figure 5, we re-plot the data from Figure 4 reordered by  $\log(\text{O/H})$  instead of by galactocentric radius. As in Figure 4, the top two panels show the results from our new C II  $\lambda 4267$  observations and the bottom plot shows the N/O values presented in Croxall et al. (2016). The top two panels of Figure 5 reproduce the trends seen in Figure 4, with a significant slope in  $\log(\text{C/O})$  and relatively constant values of  $\log(\text{C/N})$ .

However, the bottom plot in Figure 5 reveals something potentially very interesting. As in Figure 4, the points where we have detected C II  $\lambda 4267$  are indicated in black and the other points from Croxall et al. (2016)

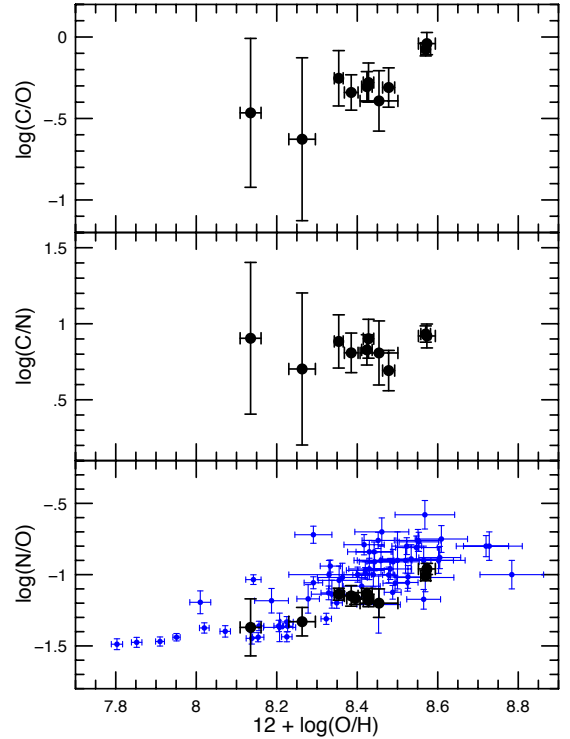


FIG. 5.— Abundances of C/O, C/N, and N/O plotted versus O/H in M 101. As in Figure 4 the top two panels show the results from our C II  $\lambda 4267$  observations and the bottom plot shows the N/O values presented in Croxall et al. (2016). In the bottom plot, the points where we have detected C II  $\lambda 4267$  are indicated in black and the other points from Croxall et al. (2016) are indicated in blue. The bottom plot shows that the regions detected in C II  $\lambda 4267$  cover a somewhat limited range in O/H and are located preferentially at lower values of N/O for a given O/H.

are indicated in blue. The bottom plot shows that the regions detected in C II  $\lambda 4267$  cover a somewhat limited range in O/H, i.e., although the last measured point in radius is very near the radial limit of the observations, there are several H II regions with lower values of O/H extending roughly 0.3 dex lower than the last measured point with a C II  $\lambda 4267$  detection. This is likely simply due to the bias of weakening C II  $\lambda 4267$  emission at lower values of O/H. An interesting impression from Figure 5 is the distribution of C II  $\lambda 4267$  detection points relative to the rest of the H II regions. Clearly N/O shows a large scatter, but the C II  $\lambda 4267$  detection points all appear to be located preferentially at lower values of N/O for a given O/H. These points tend to delineate the lower bound in N/O in the N/O versus O/H plot. Given that the C II  $\lambda 4267$  detections represent the highest surface brightness (and typically the youngest) H II regions, this might either represent an observational bias or something more physical like a lack of nitrogen pollution in the youngest objects.

In a comparison of CHAOS observations of four spiral galaxies, Berg et al. (2020) found a strong trend such that the H II regions with the lowest N/O ratios at a given value of O/H had the highest values of the  $\text{O}^{+2}$  fractional ionization,  $\text{O}^{+2}/(\text{O}^{+} + \text{O}^{+2})$ . If the high values of the  $\text{O}^{+2}$  fractional ionization are indicative of the youngest ionizing stellar clusters, then the higher values of N/O in H II regions with lower  $\text{O}^{+2}$  fractional ionization (and thus, indicative of older age stellar ion-

izing clusters) might be simply understood in terms of localized nitrogen pollution (e.g. Kobulnicky et al. 1997). Note that this trend is opposite to the original suggestion of Garnett (1990) that low values of N/O are indicative of recent pollution by supernovae which are then followed by higher values of N/O when the nitrogen production of intermediate mass stars has had a chance to catch up.

### 5.2. On the Origins of Carbon

Insights into the nucleosynthesis of the elements is often provided by trends in relative and/or absolute abundances. The relatively constant value of C/N over a large range in metallicity remains a confounding challenge to chemical evolution theories which require a fine tuning of the contributions of C from massive and intermediate mass stars to match the nucleosynthesis of N which comes predominantly from the CNO process at the metallicities typical of spiral galaxies.

Esteban et al. (2019) have gathered the literature data for five spiral galaxies with nebular carbon abundance measurements and find a variety of C/H abundance gradients as a function of  $R_e$ . In the future, the CHAOS project has the potential to double the number of galaxies with measured C/H abundance gradients and perhaps comparisons of the C, N, and O abundances in these galaxies with different chemical evolutionary histories will provide better insight into the nucleosynthetic origins of carbon.

## 6. CONCLUSIONS

CHAOS project LBT/MODS observations of H II regions in M101 have resulted in detections of the C II  $\lambda 4267$  recombination line in ten regions. These observations are in excellent agreement with the previously published observations for six regions in M101.

We use a newly calculated ionization correction factor for  $C^{++}/H^+$  to convert our  $C^{++}$  abundances to total C abundances.

These new observations allow us to provide secure measurements of the C/H and C/O gradients in M101. The C/H gradient in M101 is relatively steep with a slope in  $\log(C/H)$  of  $-0.37 \pm 0.06 \text{ dex } R_e^{-1}$ , in good agreement with the previous measurements by Esteban et al. (2009, 2019). The C/N observations are consistent with a constant value of  $\log(C/N) = 0.84$  with a dispersion of only 0.09 dex. The constant C/N ratio over a large range in metallicity (0.5 dex) is challenging to understand, given the different nucleosynthetic sources of C and N.

When plotted as a function of O/H, the trends in C/O and C/N are quite similar to what is seen in the radial gradients. That C/N is relatively constant implies that C/O and N/O should be similar. The large number of N/O observations show a flattening at large radii while the current C/O observations are insufficient to significantly constrain the trend for the outer H II regions. Additional observations of C in the outer H II regions of

M101 will be very useful in this regard.

We also note that when plotting N/O versus O/H, all of the H II regions with detections of C II  $\lambda 4267$  present N/O abundances at the minimum of the scatter in N/O at a given value of O/H. If this is not the result of an observational bias, and if the high surface brightness necessary for the detection of the faint recombination lines is interpreted as an indicator of H II region youth, then this may point to a lack of nitrogen pollution in the youngest H II regions.

Due to the extreme weakness of the carbon recombination lines, our contribution represents a valuable addition to the study of carbon in the ISM of spiral galaxies. In the future, we will analyze and publish additional C II emission line detections from other galaxies in the CHAOS project.

This work has been supported by NSF Grants AST-1109066 and AST-1714204. E.D.S. is extremely grateful for the opportunity to attend the Second Workshop “Chemical Abundances in Gaseous Nebulae: Open Problems in Nebular Astrophysics” held at the Universidade do Vale do Paraiba, Brazil, in March 2019 where he learned many things important to the development of this paper. We thank the anonymous referee for a very prompt and insightful report which we believe significantly improved this paper. This paper uses data taken with the MODS spectrographs built with funding from NSF grant AST-9987045 and the NSF Telescope System Instrumentation Program (TSIP), with additional funds from the Ohio Board of Regents and the Ohio State University Office of Research. This paper made use of the modsIDL spectral data reduction pipeline developed in part with funds provided by NSF Grant AST-1108693. We are grateful to D. Fanning, J. X. Prochaska, J. Henawi, C. Markwardt, and M. Williams, and others who have developed the IDL libraries of which we have made use: coyote graphics, XIDL, idlutils, MPFIT, and impro. This work was based in part on observations made with the Large Binocular Telescope (LBT). The LBT is an international collaboration among institutions in the United States, Italy and Germany. The LBT Corporation partners are: the University of Arizona on behalf of the Arizona university system; the Istituto Nazionale di Astrofisica, Italy; the LBT Beteiligungsgesellschaft, Germany, representing the Max Planck Society, the Astrophysical Institute Potsdam, and Heidelberg University; the Ohio State University; and the Research Corporation, on behalf of the University of Notre Dame, the University of Minnesota, and the University of Virginia. This research has made use of the NASA/IPAC Extragalactic Database (NED) which is operated by the Jet Propulsion Laboratory, California Institute of Technology, under contract with the National Aeronautics and Space Administration and the NASA Astrophysics Data System (ADS).

## REFERENCES

- Arnett, D. 1996, *Supernovae and Nucleosynthesis: An Investigation of the History of Matter, from the Big Bang to the Present*, Princeton: Princeton University Press
- Berg, D. A., Croxall, K. V., Skillman, E. D., Pogge, R. W., Moustakas, J., Groh-Johnson, M., 2015, *ApJ*, 806, 16
- Berg, D. A., Skillman, E. D., Henry, R. B. C., Erb, D. K., Berg, D. A., Erb, D. K., Henry, R. B. C., Skillman, E. D., & McQuinn, K. B. W. 2019, *ApJ*, 874, 93
- Berg, D. A., Pogge, R. W., Skillman, E. D., et al. 2020, arXiv e-prints, arXiv:2001.05002

- Binette, L., Matadamas, R., Hägele, G. F., Nicholls, D. C., Magris C., G., Peña-Guerrero, M.Á., Morisset, C. & Rodríguez-González, A. 2012, *A&A*, 547A, 29
- Bresolin, F. 2007, *ApJ*, 656, 186
- Bresolin, F., Ryan-Weber, E., Kennicutt, R. C., & Goddard, Q. 2009, *ApJ*, 695, 580
- Bundy, K., Bershad, M. A., Law, D. R., et al. 2015, *ApJ*, 798, 7
- Bryant, J. J., Owers, M. S., Robotham, A. S. G., et al. 2015, *MNRAS*, 447, 2857
- Carigi, L., Peimbert, M., Esteban, C., & García-Rojas, J. 2005, *ApJ*, 623, 213
- Croxall, K. V., Pogge, R. W., Berg, D. A., Skillman, E. D., & Moustakas, J. 2016, *ApJ*, 830, 4
- Davey, A. R., Storey, P. J., & Kisielius, R. 2000, *A&AS*, 142, 85
- Esteban, C., Peimbert, M., Torres-Peimbert, S., & Escalante, V. 1998, *MNRAS*, 295, 401
- Esteban, C., Peimbert, M., Torres-Peimbert, S., & Rodríguez, M. 2002, *ApJ*, 581, 241
- Esteban, C., García-Rojas, J., Peimbert, M., et al. 2005, *ApJ*, 618, L95
- Esteban, C., Bresolin, F., Peimbert, M., García-Rojas, J., Peimbert, A., & Mesa-Delgado, A. 2009, *ApJ*, 700, 654
- Esteban, C., García-Rojas, J., Carigi, L., et al. 2014, *MNRAS*, 443, 624
- Esteban, C., Bresolin, F., García-Rojas, J., & Toribio San Cipriano, L., 2019, *MNRAS*, 491, 2137
- Ferrarese, L., Ford, H. C., Huchra, J., et al. 2000, *ApJS*, 128, 431
- Feuillet, D. K., Bovy, J., Holtzman, J., et al. 2018, *MNRAS*, 477, 2326
- García-Rojas, J., & Esteban, C. 2007, *ApJ*, 670, 457
- Garnett, D. R. 1990, *ApJ*, 363, 142
- Garnett, D. R. 1992, *AJ*, 103, 1330
- Garnett, D. R., Skillman, E. D., Dufour, R. J., et al. 1995, *ApJ*, 443, 64
- Garnett, D. R., Skillman, E. D., Dufour, R. J., & Shields, G. A. 1997, *ApJ*, 481, 174
- Garnett, D. R., Shields, G. A., Peimbert, M., et al. 1999, *ApJ*, 513, 168
- Hasselquist, S., Holtzman, J. A., Shetrone, M., et al. 2019, *ApJ*, 871, 181
- Henry, R. B. C., Edmunds, M. G., & Köppen, J. 2000, *ApJ*, 541, 660
- Henry, R. B. C., Stephenson, B. G., Miller Bertolami, M. M., Kwitter, K. B., & Balick, B. 2018, *MNRAS*, 473, 241
- Hill, J. M. 2010, *Appl. Opt.*, 49, D115
- Hirschi, R., Meynet, G., & Maeder, A. 2005, *A&A*, 433, 1013
- Ho, I.-T., Seibert, M., Meidt, S. E., et al. 2017, *ApJ*, 846, 39
- Hodge, P. W., Gurwell, M., Goldader, J. D., Kennicutt, R. C., Jr. 1990, *ApJS*, 73, 661
- Hummer, D. G. & Storey, P. J. 1987, *MNRAS*, 224, 801
- Izotov, Y. I., & Thuan, T. X. 1999, *ApJ*, 511, 639
- Jenkins, E. B. 2004, *Origin and Evolution of the Elements*, 336
- Kewley, L. J. & Ellison, S. L., 2008, *ApJ*, 681, 1183
- Kennicutt, R. C. Jr., Bresolin, F., & Garnett, D. R. 2003, *ApJ*, 591, 801
- Kennicutt, R. C. Jr. et al. 2011, *PASP*, 123, 1347
- Kobulnicky, H. A., Skillman, E. D., Roy, J.-R., et al. 1997, *ApJ*, 477, 679
- Kreckel, K., Ho, I.-T., Blanc, G. A., et al. 2019, *ApJ*, 887, 80
- Law, D. R. et al. 2015, *AJ*, 150, 19
- Li, Y., Bresolin, F., & Kennicutt, R. C. Jr. 2013, *ApJ*, 766, 17
- Maeder, A. 1992, *A&A*, 264, 105
- Meynet, G., & Maeder, A. 2002, *A&A*, 390, 561
- Moustakas, J. & Kennicutt, R. C. Jr 2006, *ApJ*, 651, 155
- Moustakas, J., Kennicutt, R. C., Jr., Tremonti, C. A., et al. 2010, *ApJS*, 190, 233
- Nissen, P. E., Chen, Y. Q., Carigi, L., Schuster, W. J., & Zhao, G. 2014, *A&A*, 568, A25
- Peimbert, M. 1967, *ApJ*, 150, 825
- Peimbert, M., & Costero, R. 1969, *Bol. Obs. Tonantzintla Tacubaya*, 5, 3
- Peimbert, A., Peimbert, M., Ruiz, M. T. 2005, *ApJ*, 634, 1056
- Pequignot, D., Petitjean, P., & Boisson, C. 1991, *A&A*, 251, 680
- Pogge, R. W., Atwood, B., Brewer, D. F., et al. 2010, *Proc. SPIE*, 77350A
- Rosales-Ortega, F. F., Kennicutt, R. C., Sánchez, S. F., et al. 2010, *MNRAS*, 405, 735
- Rosolowsky, E. & Simon, J. D. 2008, *ApJ*, 675, 1213
- Sánchez, S. F., Rosales-Ortega, F. F., Marino, R. A., et al. 2012, *A&A*, 546, A2
- Sánchez, S. F., Rosales-Ortega, F. F., Iglesias-Páramo, J., et al. 2014, *A&A*, 563, A49
- Sánchez-Menguiano, L., Sánchez, S. F., Pérez, I., et al. 2016, *A&A*, 587, A70
- Sánchez-Menguiano, L., Sánchez, S. F., Pérez, I., et al. 2018, *A&A*, 609, A119
- Simón-Díaz, S., & Stasińska, G. 2011, *A&A*, 526, A48
- Skillman, E. D., Kennicutt, R. C., Jr., Shields, G. A., & Zaritsky, D. 1996, *ApJ*, 462, 147
- Stasińska, G. 2005, *A&A*, 434, 507
- Stasińska, G., Morisset, C., Simón-Díaz, S., et al. 2013, *A&A*, 551, A82
- Strauss, M. A., Weinberg, D. H., Lupton, R. H., et al. 2002, *AJ*, 124, 1810
- Toribio San Cipriano, L., García-Rojas, J., Esteban, C., Bresolin, F., & Peimbert, M. 2016, *MNRAS*, 458, 1866
- Toribio San Cipriano, L., Domínguez-Guzmán, G., Esteban, C., et al. 2017, *MNRAS*, 467, 3759
- Tremonti, C. A., Heckman, T. M., Kauffmann, G., et al. 2004, *ApJ*, 613, 898
- van den Hoek, L. B., & Groenewegen, M. A. T. 1997, *A&AS*, 123, 305.
- Walter, F., Brinks, E., de Blok, W. J. G., Bigiel, F., Kennicutt, R. C., Jr., Thornley, M. D., & Leroy, A. 2008, *AJ*, 136, 2563
- Woosley, S. E. & Weaver, T. A. 1995, *ApJS*, 101, 181
- Zaritsky, D., Kennicutt, R. C., Jr., & Huchra, J. P. 1994, *ApJ*, 420, 87